Ultrafast Internal Exciton Dissociation through Edge States in MoS$_2$ Nanosheets with Diffusion Blocking

Xinyu Sui,[†] Huimin Wang,[†] Cheng Liang,[†] Qing Zhang, Han Bo, Keming Wu, Zhuoya Zhu, Yiyang Gong, Shuai Yue, Hailong Chen, Qiuyu Shang, Yang Mi, Peng Gao, Yong Zhang,* Sheng Meng,* and Xinfeng Liu*
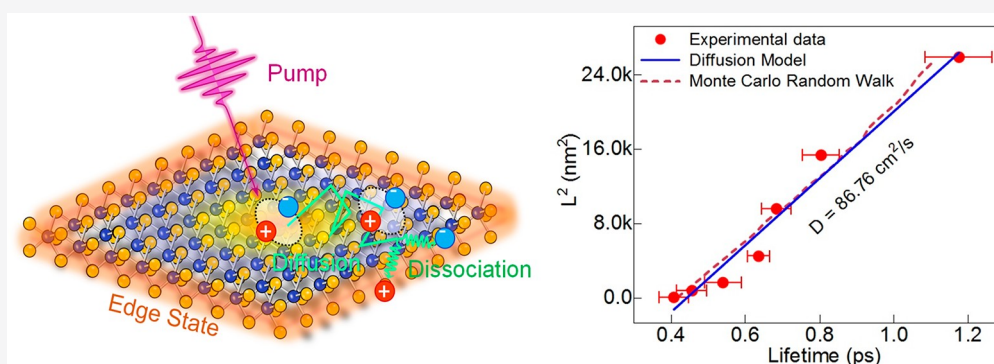
Read Online

ACCESS | Metrics & More | Article Recommendations | Supporting Information

ABSTRACT: Edge states of two-dimensional transition-metal dichalcogenides (TMDCs) are crucial to quantum circuits and optoelectronics. However, their dynamics are pivotal but remain unclear due to the edge states being obscured by their bulk counterparts. Herein, we study the state-resolved transient absorption spectra of ball-milling-produced MoS$_2$ nanosheets with 10 nm lateral size with highly exposed free edges. Electron energy loss spectroscopy and first-principles calculations confirm that the edge states are located in the range from 1.23 to 1.78 eV. Upon above bandgap excitations, excitons populate and diffuse toward the boundary, where the potential gradient blocks excitons and the edge states are formed through interband transitions within 400 fs. With below bandgap excitations, edge states are slowed down to 1.1 ps due to the weakened valence orbital coupling. These results shed light on the fundamental exciton dissociation processes on the boundary of functionalized TMDCs, enabling the ground work for applications in optoelectronics and light-harvesting.

KEYWORDS: MoS$_2$ nanosheets, Edge states, Carrier dynamics, Exciton dissociation, Diffusion blocking

The surface states of bulk condensates have long been the research focus due to intriguing physical and chemical properties.[1−5] In the past few decades, two-dimensional (2D) transition-metal dichalcogenides (TMDCs) with a monolayer or a few layers have shown significant progress in the fields of electronics, nanophotonics, spintronics, plasmonics, and nano-catalysis.[6−11] Analogous to the surface state in bulk solids, edge states of 2D TMDCs triggered by translational symmetry breaking and edge polar discontinuities attracted broad and long-lasting interest,[12−14] such as edge conduction, edge plasmons,[15−17] spin protected transport,[18−20] Luttinger liquid behavior,[21] and high catalytic activity.[22] These remarkable edge properties spark new opportunities for basic research and applications of TMDCs.

Electronic states on the edges of TMDCs have been partially revealed with characteristics containing sub-bandgap distributions,[23−25] metallic bands,[23,26−28] spin nondegeneracy,[19,20] and terminal localization.[23,28−31] However, their dynamics have not

been fully understood, especially how and how fast edge states populate, and how they contribute to overall charge transport and recombination. Addressing these questions is critical for optimizing and extending TMDC applications, but it remains a challenge, because the weak edge signals are usually drowned out by interior backgrounds or disturbed by edge impurities.[32] Extremely exposed and clean edge structures are highly desired. Recent research efforts including thermal annealing,[33] vapor−liquid−solid growth,[34] and nanowire embedding in different layered materials[35,36] bring out opportunities to enhance the edge signal for experimental detections.
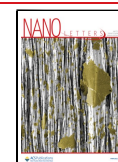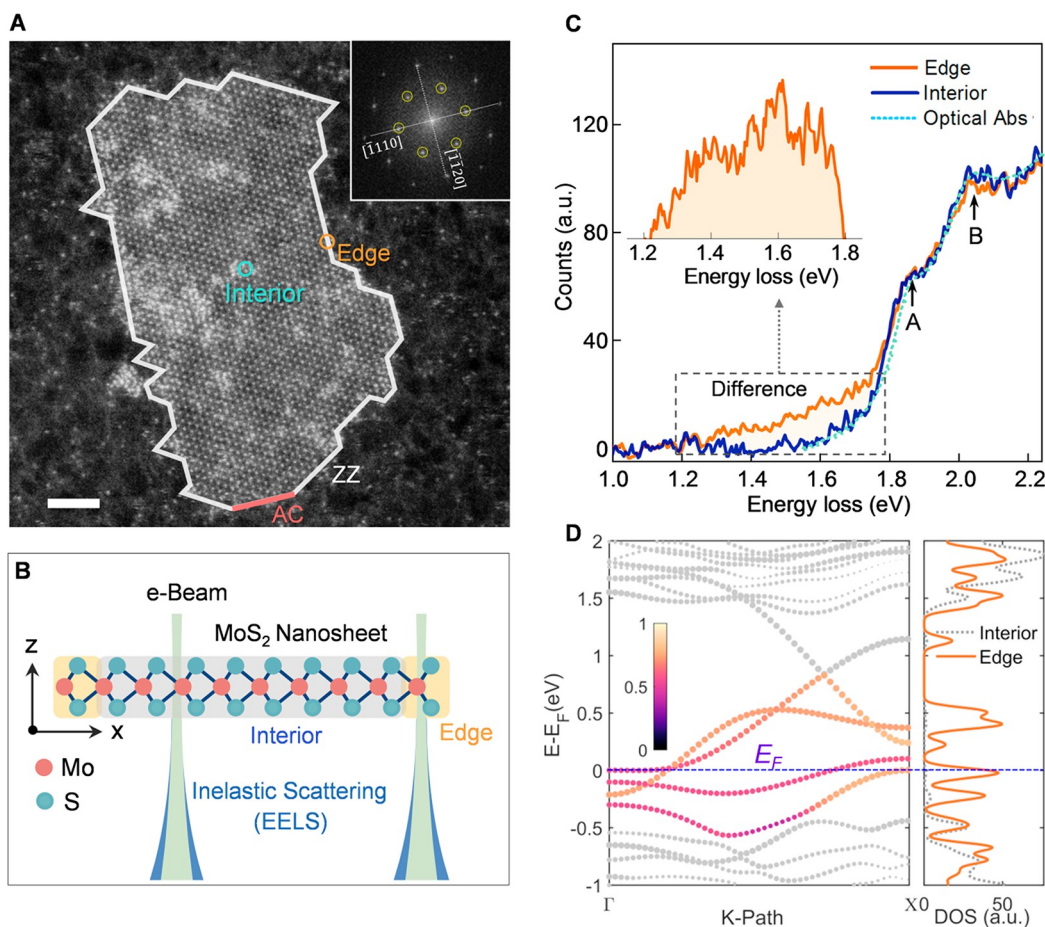
Figure 1. EELS measurement of edge states in a single MoS$_2$ nanosheet. (A) Typical HAADF-STEM images of MoS$_2$ nanosheets. The inset shows the corresponding FFT pattern. Hexagonal diffraction spots are marked by yellow circles. Armchair [$\bar{1}$110] and zigzag [$\bar{1}$120] directions are labeled, respectively. (B) Scheme of EELS measurement on single MoS$_2$ nanosheet. (C) EELS at interior and edge site of MoS$_2$ nanosheet. Optical absorption is given as a reference. Absorptions of A and B excitons are marked, respectively. The inset highlights the edge state absorption ranging from 1.23 to 1.78 eV, centered at 1.52 eV. (D) Electronic band structure (left) from MoS$_2$ zigzag edge calculated by DFT. Energy bands across the Fermi level (blue dashed line) are emphasized in color. Total DOS of MoS$_2$ zigzag edge (right) compared with DOS of interior site (gray dashed line).

Herein, we reveal edge state population dynamics and population competition with an exciton using ball-milling-produced 10 nm MoS$_2$ nanosheets with high zigzag edges exposed. Combined with electron energy loss spectroscopy (EELS) and first-principles calculations, we identify the as-predicted sub-bandgap edge state absorption covering from 1.23 to 1.78 eV. Due to their nanometer size, these nanosheets have highly exposed edges, accounting for ∼11% of the sheet area, facilitating the direct transient absorption (TA) study for edge states. With above bandgap excitations, photoexcited excitons first populate and soon dissociate into edge electronic states within ∼0.40 ps via interband transitions. With below bandgap excitations, the edge state has a longer population time up to 1.0 ps, which is due to reduced intraband orbital coupling through nonadiabatic coupling (NAC) analysis. Moreover, we find that the edge state introduces the external potential gradient on the boundary, terminating exciton diffusive transport of the exciton from interior. We extract the exciton diffusion coefficient of 86.7 cm^2/s through measuring exciton dissociation lifetime as a function of nanosheet lateral size. These results expand the understanding of edge state dynamics in TMDC semiconductors from energy,

temporal, and spatial perspectives, providing a pathway for edge state manipulation and device optimization.

The high quality MoS$_2$ nanosheets with size gradient (10–160 nm) were prepared with a silica-assisted ball-milling method based on our previous work.[37] Their intrinsic MoS$_2$ properties are confirmed via absorption spectroscopy and Raman spectroscopy (Supporting Information, Figures S1–S4). Figure 1A shows the high angle annular dark field scanning transmission electron microscopy (HAADF-STEM) of a typical MoS$_2$ nanosheet with size around 10 nm. The corresponding FFT pattern (inset) demonstrated solely one set of hexagonal diffraction spots, indicating a high lattice quality without domains. The first order diffraction spots are marked with a yellow circle, through which the [$\bar{1}$110] armchair and [$\bar{1}$120] zigzag directions are assigned, respectively. It can be found that MoS$_2$ nanosheets are mainly surrounded by zigzag edges (marked as white, for details see Supporting Information, Figure S5). The reason lies in that the low formation energy zigzag edge leads to its cracking advantage under mechanical strain in ball-milling.[38,39]

We start by using EELS to confirm the existence of edge states. The schematic of EELS is illustrated in Figure 1B. In order to minimize the damage of the electron beam to MoS$_2$
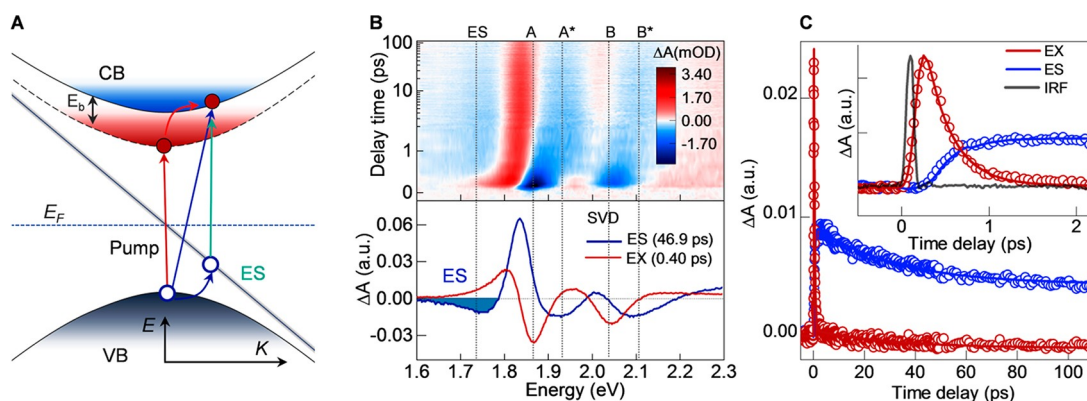
Figure 2. Edge state dynamics with band edge resonant excitation. (A) Energy diagram of exciton and edge state. The exciton was first created by resonant excitation. Then, the hole hoop to the edge state band has the energy transfer to the conductive electrons to overcome the binding energy. (B) 2D pseudocolor plot of TA spectra with 1.87 eV excitation (resonant with A exciton) and fluence of 4.0 $\mu J/cm^2$. The exciton (noted as EX) related component via SVD in the red line shows the lifetime of 0.40 ps. The edge state (noted as ES) related component via SVD in the blue line shows the lifetime of 46.9 ps. (C) The temporal evolution of the exciton state (noted as EX) and edge state (noted as ES) via SVD and their global fittings. The inset highlights the correlated rise and decay process between the edge state and exciton.

nanosheets, the beam metering was reduced to 1% of that in scanning transmission electron microscope (STEM) mode by a slit diaphragm.[40] The electron energy loss induced by inelastic electron scattering gives information on different excitations in materials such as phonons, excitons, and plasmons. For thin materials, EELS can be directly compared to optical absorption because it measures the imaginary part of the dielectric function.[41−43] Figure 1C shows the EELS for the interior and edge site, respectively. Additional optical absorption of MoS_2 nanosheets is given as reference. Transitions of the A exciton (1.87 eV) and B exciton (2.04 eV) are clearly identified and marked with arrows.[9] It can be found that edge EELS, interior EELS, and the optical absorption spectrum are identical in the above bandgap region, confirming the accuracy of EELS. In the below bandgap region, the edge state absorption tail is featured. With the EELS difference extracted between the edge and interior, the edge absorption is strengthened in the inset of Figure 1C, ranging from 1.23 to 1.78 eV, centered at 1.52 eV. As zigzag edges dominate as discussed above, edge EELS is contributed by the zigzag edge states. Figure 1D shows the DFT calculated energy bands and total density of states (DOS) on the zigzag edge via an infinite 2D nanoribbon, which provides more insights. First, color-rendered energy bands of edge states (left side) are across the Fermi level, suggesting metallic characteristics consistent with previous reports. Second, the total DOS (right side) on the zigzag edge shows the abundant sub-bandgap distributions compared with the interior DOS, explaining the sub-bandgap edge absorption in EELS. The edge state absorption peak is theoretically predicted to be located at 0.67 times the absorption peak of the A exciton.[44] The EELS measured edge absorption (1.52 eV) here is higher than the theoretically predicted value (1.25 eV), considering the A exciton of 1.87 eV. It is presumably due to the possible self-energy correction or plasmon effects.[16,45]

Highly exposed edge structures in 10 nm nanosheets are found to occupy an 11% sheet area (Supporting Information, Figure S6A), which is conductive for resolving edge state population dynamics via TA spectroscopy. The ratio of edge states to A excitons in the TA signal decreases with increasing lateral size (Supporting Information, Figure S6B), which confirms the correlation between macroscopic TA properties

and microscopic edges. Figure 2A summarizes the energy diagram and gives potential transition pathways between the edge state and the exciton. The metallic edge bands are simplified to a linear dispersion band according to the previously reported analytical model.[19,44] We will show below that the valence band hole of the exciton upon photoexcitation would transfer to the edge state band through an interband transition, which subsequently led the conductive electron free from exciton binding energy. Videlicet, the excitons are dissociated via edge states and free carriers are subsequently generated.

The 2D pseudocolor TA mapping is shown in Figure 2B with photoexcitation that is resonant at the A exciton transition (pump with 1.87 eV, ∼100 fs, 4.0 $\mu J/cm^2$). The bleaching of A (1.87 eV) and B (2.04 eV) excitons is first established, with energies consistent with EELS results. Accompanied by the decay of the A and B excitons, an additional three bleach peaks, respectively, located at 2.11, 1.94, and 1.75 eV, are subsequently established. The bleach peak at 1.75 eV within the edge absorption band (1.23−1.78 eV) is assigned as an edge state. Other assignments such as the trap state are eliminated through near-IR TA (Supporting Information, Note S1), where no distributed trap induced broad bleaches are observed (Supporting Information, Figure S7).[46] Meanwhile, no obvious fluorescence signal from defect-trapped excitons was observed at 77 K (Figure S8), indicating that the influence of defect states can be neglected in our case. The singular value decomposition (SVD) method (Supporting Information, Note S2) is performed to clearly separate multispectral components according to their individual dynamics. Here, two spectral components including the exciton and the edge state are, respectively, separated in the bottom panel of Figure 2B. Their individual dynamics shown in Figure 2C will be discussed latter. The exciton component (red plot, with bleach peak at 1.87 and 2.04 eV) shows a 0.40 ps decay lifetime. The edge state component (blue plot, with three bleach peaks at 2.11, 1.94, and 1.75 eV) shows a 42.6 ps decay lifetime. In the edge state component, two peaks at 1.94 and 2.11 eV labeled as A* and B* both show a ∼70 meV blue shift from the A and B excitons. This is the signature of free carriers free from exciton binding energy in few-layer MoS_2.[47] The assignments of free charges are supported by two pieces of evidence. One is the
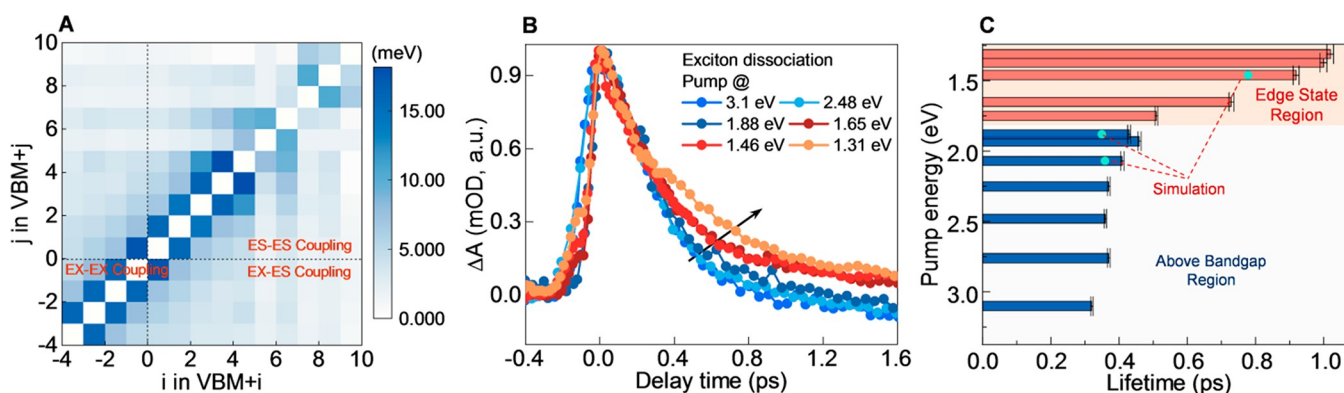
Figure 3. Energy dependent edge state dynamics. (A) NAC matrix of K−S orbital coupling of the exciton states (noted as EX) and edge state (noted as ES). (B) The excitation energy dependent exciton decay dynamics, corresponding to the edge state formation. (C) Edge state formation lifetime as a function of pump energy. The blue region represents above bandgap excitation. The red region represents sub-bandgap excitation within the edge absorption region.

biomolecule recombination feature in power dependent TA spectroscopies (Supporting Information, Note S3 and Figure S9). Another is the characteristic Drude absorption feature in mid-IR TA spectroscopies (Supporting Information, Note S4 and Figure S10). As is illustrated in Figure 2A, the free carrier bleaches appearing in the edge state component suggest that the edge state and free carriers share the same conductive electrons. Figure 2C reveals the population dynamics of the exciton and edge state, respectively. The decay lifetimes of exciton and edge state are fitted as 0.40 and 42.6 ps, which are labeled in Figure 2B. The inset of Figure 2C shows a zoom in perspective, clearly illustrating the population buildup of the exciton and edge state, respectively. Excitons are occupied within 0.15 ps close to the instrument response limit. In a comparison with the exciton, the edge state shows a delayed population onset. Global fittings (Supporting Information, Note S3) illustrate that the edge state population is fully provided from the exciton decay within ∼0.4 ps, which is derived by the interband transition of the photoexcited hole in the exciton band to edge state band according to the energy diagram in Figure 2A. This is a noteworthy result in that the ultrafast exciton dissociation can be comparable to the fastest results in other hetero-nanostructures (Supporting Information, Table S1), which reveals the potential applications in optoelectronic devices, energy conversion, nanocatalysis, etc.

Excitation energy dependent edge state population dynamics are studied with a combination of ab initio nonadiabatic molecular dynamics (NAMD) and pump energy dependent TA spectroscopies. In NAMD, nonadiabatic coupling (NAC) is introduced (Figure 3A) to quantize the orbital coupling throughout the exciton band to the edge state band (Supporting Information, Note S5). NAC matrix element d_{ij} describes the hole Kohn−Sham (KS) orbital (with index i and j) coupling strength which started from the Fermi energy (noted as VBM + 10) and ended below the VBM (noted as VBM − 4), where the VBM (valence band maximum) locates at the bulk band edge position. The NAC matrix in Figure 3A can be divided into three regions (I−III) due to exchange symmetry. Region I represents exciton−exciton coupling, corresponding to the exciton cooling process in above bandgap excitation. Region II represents exciton−edge state coupling corresponding to exciton dissociation triggered edge state occupation. Region III represents edge state intraband relaxation in below bandgap excitations. In regions I−III, the

strongest orbital couplings always occur at the subdiagonal position standing to adjacent orbital coupling, which suggests cascade relaxation from the high energy exciton to low energy edge states. Subdiagonal NAC elements decrease as the hole KS orbital gradually approaches the Fermi energy (VBM + 10) (Supporting Information, Figure S11), indicating that edge state relaxation would be slowed with decreasing pump energy which is supported by experimental evidence as described below.

TA spectroscopies with pump energy from 3.10 to 1.31 eV are taken (Supporting Information, Figure S12) in line with regions I−III of the NAC matrix. In these spectra, the SVD and global fitting results (Supporting Information, Figure S13−S14) show that edge state formation is always associated with exciton decay, which could be well-explained from the relaxation pathways under above or below bandgap excitations. In above bandgap excitations, the edge state originating from an interband transition triggered exciton dissociation is discussed above. In below bandgap excitations, this is due to the intraband relaxation between the metastable edge state and stable edge state (see schematic in Supporting Information, Figure S15), where the metastable edge state and excitons share the same conductive electrons resulting from exciton bleach. Figure 3B shows the energy dependent edge state formation process illustrated by exciton decay, showing the slow formation trend with a reduced pump energy. Figure 3C fully summarizes the pump energy dependent edge state formation lifetimes. In the above bandgap region (pump energy from 3.10 to 1.87 eV), occupation of the edge state is around 0.40 ps. The slight acceleration of population buildup under a high energy pump is presumably caused by the dispersed distribution of off-diagonal coupling in region II. With sub-bandgap excitation in the edge state absorption band (pump energy from 1.75 to 1.31 eV), edge state formation shows the slowing trend from 0.6 to 1.1 ps. It is due to the reduction of the KS orbital coupling in region III illustrated in Figure S11. Three typical pump energies of 1.99, 1.87, and 1.62 eV are selected to simulate the edge state formation process via NAMD, corresponding to the above bandgap, band edge resonant, and below bandgap excitations, respectively (Supporting Information, Figure S16). The simulated dynamics are fitted and superimposed in Figure 3C, showing good agreements with experimental values, and indicating that the
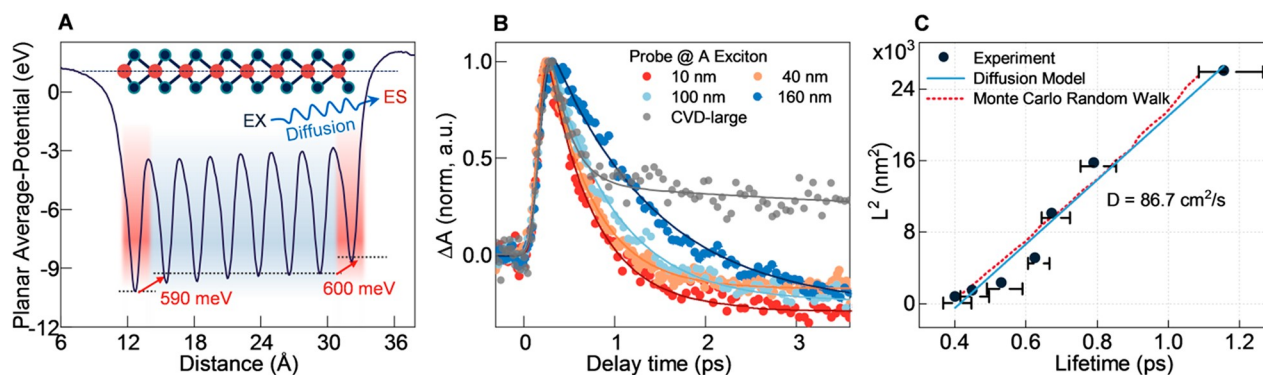
Figure 4. Diffusion limited edge state formation. (A) DFT calculated local potential profile across the nanosheet. The potential gradient is localized in the edge site with 0.4 nm, trapping the exciton on edge into edge states via dissociation. (B) Exciton dissociation as a function of nanosheet average size. (C) The square of lateral size as a function of exciton lifetime, showing a diffusion induced linear dependence. The diffusion coefficient with 86.7 cm²/s is verified via diffusion model fitting and a random walk simulation through the Monte Carlo method, respectively.

orbital coupling maximally determines the pump energy dependent edge state population dynamics.

The influence of exciton transport for edge state population dynamics was further studied. The average potential profile along the section of MoS_2 nanoribbon with a zigzag edge (Figure 4A) is calculated, where the left side ends with S, and the right side ends with Mo. In sharp contrast with the interior region, the S and Mo end terminals show the average potential gradient with ~590 and ~600 meV, respectively, which is reported from polar discontinuities.[12−14,28,45] The interior exciton is expected to be trapped by the edge potential when arriving at the edge terminal. Hence, the exciton dissociation induced edge state population is expected to be limited by exciton diffusion toward the boundary. To verify this inference, we take TA spectroscopies for samples with lateral sizes from 10 to 160 nm (Supporting Information, Figures S17 and S18) with band edge resonant excitation (1.87 eV, 4.0 $\mu J/cm^2$). Figure 4B shows the exciton dissociation dynamics in nanosheets with typical sizes of 10, 41, 98, and 160 nm. With the lateral size increasing from 10 to 160 nm, the exciton lifetime is slowed down from 0.4 to 1.2 ps, which is faster than the defect scattering. As a comparison, intrinsic exciton decay is obtained by ~4 ps from the pristine monolayer MoS_2 grown by CVD.[48] Figure 4C illustrates the second power of nanosheet lateral size as a function of exciton dissociation lifetime. Their linear relationship could be well-described by a classical diffusion model with a diffusion coefficient of 86.7 cm²/s (Supporting Information, Note S6). Moreover, we simulate an exciton random walk with edge termination via the Monte Carlo method (Supporting Information, Figure S19−S20) to verify the diffusion coefficient from another perspective. Both the classical diffusion model and random walk results show a consistent diffusion coefficient of 86.7 cm²/s, further confirming the boundary blocked exciton diffusion. This diffusion coefficient is on the same order of magnitude but is larger than the previously reported value (20 ± 10 cm²/s),[49] which may originate from low cumulative defect scattering or hot phonon drag on short diffusion scales.[50] MoS_2 nanosheets with lateral sizes of 10−160 nm are far less than the natural exciton diffusion length (931 nm) (Supporting Information, Table S2), which enables the exciton to entirely diffuse to the edge site instead of decaying in the interior region. Hence, exciton dissociation via the edge state is significant when the size of the nanosheet is smaller than the exciton dissociation critical length, which could also be

calculated in other kinds of TMDCs (Supporting Information, Figure S21). More importantly, we can conclude that the smaller the nanosheet lateral size is, the sooner the exciton arrives at the boundary. In particular, the diffusion time in 10 nm nanosheets is only 0.01 ps (Supporting Information, Figure S19), a negligible value compared with exciton dissociation (0.4 ps).

In summary, through ball-milling-produced MoS_2 nanosheets, the edge state is revealed with sub-bandgap absorption in 1.23−1.78 eV, and its population dynamics are systematically investigated via combined transient absorption and first-principles calculations. Compared with the heterostructure, the edge structure has the comparable performance to dissociate excitons within 0.4 ps but features in the continuous in-plane interface and one-dimensional distributions, which bring out new opportunities in optoelectronics, solar energy conversion, and optical switching. While valence orbital couplings are found to dominate the pump energy dependent edge state population, more details remain for explorations such as many body interactions, spin selective transitions and transport, external filed impacts, etc. With an increase in the nanosheet lateral size, the edge state population is found to be limited by exciton diffusive transport, which may provide insights into optimal design for the device or catalyst. The demonstrated ultrafast edge state population dynamics and its competitive relationship with the interior exciton in MoS_2 nanosheets provide a promising platform for manipulating and utilizing edge states not only for basic science but also for charge transport and separation applications.

■ MATERIALS AND METHODS

Production and Preparation MoS₂ Nanosheets. The MoS_2 nanosheets with different sizes (10−160 nm) were prepared using a previously reported modified ball-milling method with three steps containing silica-assisted ball-milling, solvent sonification exfoliation, and cascading centrifugal purification.[37] The purified MoS_2 nanosheet powder is processed by vacuum drying and redispersed in N-methyl-2-pyrrolidone (NMP, 99.5%, anhydrous) with a concentration of 0.01 mg mL⁻¹. For optical characterization in this work including Raman spectroscopy, steady state absorption, and TA, MoS_2 nanosheets are dispersed in a poly(methyl methacrylate) (PMMA) solid film. In brief, PMMA was dissolved in NMP to form a 400 mg mL⁻¹ solution by magnetic stirring overnight. Meanwhile, the MoS_2 nanosheets

with varying sizes were dispersed in NMP to form 1 mg mL^{-1} dispersions by sonication. The PMMA solution and NS dispersion (0.01 mg mL^{-1} in NMP) were mixed by vigorous stirring and sonication. The mixture was dropped into a PTFE mold (an 8 μm thick polyimide film as the releasing layer). After complete removal of the solvent from the evenly spreading mixture by moderate heating (70 °C) overnight on a hot plate, the MoS$_2$ nanosheets−PMMA thin films with were obtained. Our previous study suggested that this ball-milled method does not introduce additional defects from bulk material.[51] The defect density in these MoS$_2$ nanosheets can be comparable with the mechanical exfoliated layer around 0.5 × 10^{13} to 5 × 10^{13} cm^{-2} according to the previous reported results.[52−54]

HAADF-STEM and EELS Characterization. The high spatial resolution STEM-HAADF imaging was performed using a Nion U-HERMES 200 microscope with both a monochromator and the aberration corrector operating at 60 kV. The beam convergence semiangle was 35 mrad. The collection semiangles were set to 80−210 mrad for HAADF imaging and 80 mrad for EELS acquisitions. All the EELS experiments were carried out at room temperature.

DFT Calculations. The density functional theory (DFT) calculations were performed via the Vienna ab initio simulation package (VASP) with the Perdew-Burke-Ernzerholf (PBE) exchange-correlation functional and projector-augmented wave (PAW) pseudopotential.[55,56] The plane-wave basis set with an energy cutoff at 340 eV was applied. The structure model contains 8 Mo atoms and 16 S atoms with the lattice constant of 3.155 Å along the ribbon. Each side of the ribbon is a zigzag edge, ended with a S or Mo atom, respectively. We used a periodic boundary condition along the nanoribbon and added a vacuum layer of 10 Å on each side of the ribbon, as well as a vacuum layer of 15 Å in the 2D material normal direction, which is sufficiently large to eliminate artificial interactions between periodic images. Geometry optimization was carried out until the residual force on each atom was less than 0.02 eV/Å. We used 10 × 1 × 1 k-mesh for the structure relaxation and electronic structure calculation and 51 k-points sampling along the ribbon for the calculation of band structure. In Figure 4A of the main text, total local potential is calculated containing ionic plus Hartree plus exchange correlations.

Transient Absorption. The femtosecond TA measurements were obtained by the HELIOS commercial fs-TA system (Ultrafast Systems). Fundamental 800 nm pulses (1 kHz, 100 fs) from a Coherent Astrella regenerative amplifier were used to pump an optical parametric amplifier (Coherent, OperA Solo) to obtain the frequency-tunable pump beam across the visible region. The pump beam was severed at 500 Hz and focused at the sample with a beam waist of approximately 300 μm. A white light continuum probe beam from 430 to 775 nm (1.6 to 2.9 eV) was acquired (with a beam waist of 150 μm at the sample) by focusing a small part of the fundamental 800 nm beam on a sapphire window. The magic angle was set for polarization of the pump and probe, respectively, to avoid the anisotropic effect. Finally, considering the instrument response function of this system, the system had an ultimate temporal resolution of approximately 120 fs.

■ ASSOCIATED CONTENT

(SI) Supporting Information

The Supporting Information is available free of charge at https://pubs.acs.org/doi/10.1021/acs.nanolett.1c04987.

Additional results including singular value decomposition, global fitting for multicomponent dynamics, characteristics of bimolecule decay, AFM images, spectroscopic data, and time dependent DFT calculations (PDF)

■ AUTHOR INFORMATION

Corresponding Authors

Xinfeng Liu − *CAS Key Laboratory of Standardization and Measurement for Nanotechnology, National Center for Nanoscience and Technology, Beijing 100190, P. R. China; University of Chinese Academy of Sciences, Beijing 100049, P. R. China;* orcid.org/0000-0002-7662-7171; Email: liuxf@nanoctr.cn

Sheng Meng − *University of Chinese Academy of Sciences, Beijing 100049, P. R. China; Beijing National Laboratory for Condensed Matter Physics and Institute of Physics, Chinese Academy of Sciences, Beijing 100190, P. R. China;* orcid.org/0000-0002-1553-1432; Email: mengs@iphy.cas.cn

Yong Zhang − *University of Chinese Academy of Sciences, Beijing 100049, P. R. China; CAS Key Laboratory of Nanosystem and Hierarchical Fabrication, CAS Center for Excellence in Nanoscience, National Center for Nanoscience and Technology, Beijing 100190, P. R. China;* orcid.org/0000-0002-5914-1065; Email: zhangyong@nanoctr.cn

Authors

Xinyu Sui − *CAS Key Laboratory of Standardization and Measurement for Nanotechnology, National Center for Nanoscience and Technology, Beijing 100190, P. R. China; University of Chinese Academy of Sciences, Beijing 100049, P. R. China*

Huimin Wang − *CAS Key Laboratory of Standardization and Measurement for Nanotechnology, National Center for Nanoscience and Technology, Beijing 100190, P. R. China; Beijing National Laboratory for Condensed Matter Physics and Institute of Physics, Chinese Academy of Sciences, Beijing 100190, P. R. China; The Laboratory of Soft Matter Physics, Beijing National Laboratory for Condensed Matter Physics, Institute of Physics, Chinese Academy of Sciences, Beijing 100190, China*

Cheng Liang − *University of Chinese Academy of Sciences, Beijing 100049, P. R. China; CAS Key Laboratory of Nanosystem and Hierarchical Fabrication, CAS Center for Excellence in Nanoscience, National Center for Nanoscience and Technology, Beijing 100190, P. R. China*

Qing Zhang − *Department of Materials Science and Engineering, College of Engineering, Peking University, Beijing 100871, China;* orcid.org/0000-0002-6869-0381

Han Bo − *International Center for Quantum Materials, School of Physics and Electron Microscopy Laboratory, School of Physics, Peking University, Beijing 100871, P. R. China*

Keming Wu − *CAS Key Laboratory of Standardization and Measurement for Nanotechnology, National Center for Nanoscience and Technology, Beijing 100190, P. R. China*

Zhuoya Zhu − *CAS Key Laboratory of Standardization and Measurement for Nanotechnology, National Center for Nanoscience and Technology, Beijing 100190, P. R. China; University of Chinese Academy of Sciences, Beijing 100049, P. R. China*

Yiyang Gong − *CAS Key Laboratory of Standardization and Measurement for Nanotechnology, National Center for Nanoscience and Technology, Beijing 100190, P. R. China*

Shuai Yue − *CAS Key Laboratory of Standardization and Measurement for Nanotechnology, National Center for Nanoscience and Technology, Beijing 100190, P. R. China; University of Chinese Academy of Sciences, Beijing 100049, P. R. China*

Hailong Chen − *Electron Microscopy Laboratory, School of Physics, Peking University, Beijing 100871, P. R. China;* orcid.org/0000-0002-3456-7836

Qiuyu Shang − *Department of Materials Science and Engineering, College of Engineering, Peking University, Beijing 100871, China*

Yang Mi − *CAS Key Laboratory of Standardization and Measurement for Nanotechnology, National Center for Nanoscience and Technology, Beijing 100190, P. R. China*

Peng Gao − *International Center for Quantum Materials, School of Physics and Electron Microscopy Laboratory, School of Physics, Peking University, Beijing 100871, P. R. China;* orcid.org/0000-0003-0860-5525

Complete contact information is available at:
https://pubs.acs.org/10.1021/acs.nanolett.1c04987

Author Contributions

[†]X.S., H.W., and C.L. contributed equally to this work. X.L. led the project. X.S. performed transient absorption spectroscopy and data analysis. C.L. and Y.Z. produced all the samples. H.B. and P.G. performed and interpreted the STEM and EELS data. H. W. and S. M. carried out the DFT simulations. X.S. prepared the manuscript. All the authors discussed and commented on the manuscript.

Notes

The authors declare no competing financial interest.

■ REFERENCES

(1) Carpinelli, J. M.; Weitering, H. H.; Plummer, E. W.; Stumpf, R. Direct observation of a surface charge density wave. *Nature* **1996**, *381* (6581), 398−400.

(2) Zhang, Q.; Hu, G.; Ma, W.; Li, P.; Krasnok, A.; Hillenbrand, R.; Alu, A.; Qiu, C. W. Interface nano-optics with van der Waals polaritons. *Nature* **2021**, *597* (7875), 187−195.

(3) Li, G.; Liang, L.; Li, Q.; Pan, M.; Nascimento, V. B.; He, X.; Karki, A. B.; Meunier, V.; Jin, R.; Zhang, J.; Plummer, E. W. Role of antiferromagnetic ordering in the (1×2) surface reconstruction of $Ca(Fe_{1-x}Cox)_2As_2$. *Phys. Rev. Lett.* **2014**, *112* (7), 077205.

(4) Plummer, E. W.; Gadzuk, J. W. Surface States on Tungsten. *Phys. Rev. Lett.* **1970**, *25* (21), 1493−1495.

(5) Matzdorf, R.; Fang, Z.; Ismail; Zhang, J.; Kimura, T.; Tokura, Y.; Terakura, K.; Plummer, E. W. Ferromagnetism stabilized by lattice distortion at the surface of the p-wave superconductor Sr_2RuO_4. *Science* **2000**, *289* (5480), 746−748.

(6) Larentis, S.; Tolsma, J. R.; Fallahazad, B.; Dillen, D. C.; Kim, K.; MacDonald, A. H.; Tutuc, E. Band Offset and Negative Compressibility in Graphene-MoS_2 Heterostructures. *Nano Lett.* **2014**, *14* (4), 2039−2045.

(7) Splendiani, A.; Sun, L.; Zhang, Y.; Li, T.; Kim, J.; Chim, C.-Y.; Galli, G.; Wang, F. Emerging Photoluminescence in Monolayer MoS_2. *Nano Lett.* **2010**, *10* (4), 1271−1275.

(8) Wang, Q. H.; Kalantar-Zadeh, K.; Kis, A.; Coleman, J. N.; Strano, M. S. Electronics and optoelectronics of two-dimensional transition metal dichalcogenides. *Nat. Nanotechnol.* **2012**, *7* (11), 699−712.

(9) Wu, F.; Qu, F.; MacDonald, A. H. Exciton band structure of monolayer MoS_2. *Phys. Rev. B* **2015**, *91* (7), 075310.

(10) Ye, Z.; Sun, D.; Heinz, T. F. Optical manipulation of valley pseudospin. *Nat. Phys.* **2017**, *13* (1), 26−29.

(11) Gronborg, S. S.; Salazar, N.; Bruix, A.; Rodriguez-Fernandez, J.; Thomsen, S. D.; Hammer, B.; Lauritsen, J. V. Visualizing hydrogen-induced reshaping and edge activation in MoS_2 and Co-promoted MoS_2 catalyst clusters. *Nat. Commun.* **2018**, *9* (1), 2211.

(12) Péterfalvi, C. G.; Kormányos, A.; Burkard, G. Boundary conditions for transition-metal dichalcogenide monolayers in the continuum model. *Phys. Rev. B* **2015**, *92* (24), 245443.

(13) Silva, F. W.; Costa, A. L.; Liu, L.; Barros, E. B. Intense conductivity suppression by edge defects in zigzag MoS_2 and WSe_2 nanoribbons: a density functional based tight-binding study. *Nanotechnology* **2016**, *27* (44), 445202.

(14) Gibertini, M.; Pizzi, G.; Marzari, N. Engineering polar discontinuities in honeycomb lattices. *Nat. Commun.* **2014**, *5*, 5157.

(15) Yan, J.; Yuan, Z.; Gao, S. End and central plasmon resonances in linear atomic chains. *Phys. Rev. Lett.* **2007**, *98* (21), 216602.

(16) Andersen, K.; Jacobsen, K. W.; Thygesen, K. S. Plasmons on the edge of MoS_2 nanostructures. *Phys. Rev. B* **2014**, *90* (16), 161410−1.

(17) Rossi, T. P.; Winther, K. T.; Jacobsen, K. W.; Nieminen, R. M.; Puska, M. J.; Thygesen, K. S. Effect of edge plasmons on the optical properties of MoS_2 monolayer flakes. *Phys. Rev. B* **2017**, *96* (15), 155407−1.

(18) Vojvodic, A.; Hinnemann, B.; Nørskov, J. K. Magnetic edge states in MoS_2 characterized using density-functional theory. *Phys. Rev. B* **2009**, *80* (12), 125416−1.

(19) Enaldiev, V. V. Edge states and spin-valley edge photocurrent in transition metal dichalcogenide monolayers. *Phys. Rev. B* **2017**, *96* (23), 235429−1.

(20) Deng, X.; Li, Z.; Yang, J. One-Dimensional Magnetic Order Stabilized in Edge-Reconstructed MoS_2 Nanoribbon via Bias Voltage. *J. Phys. Chem. Lett.* **2020**, *11* (18), 7531−7535.

(21) Yang, G.; Shao, Y.; Niu, J.; Ma, X.; Lu, C.; Wei, W.; Chuai, X.; Wang, J.; Cao, J.; Huang, H.; Xu, G.; Shi, X.; Ji, Z.; Lu, N.; Geng, D.; Qi, J.; Cao, Y.; Liu, Z.; Liu, L.; Huang, Y.; Liao, L.; Dang, W.; Zhang, Z.; Liu, Y.; Duan, X.; Chen, J.; Fan, Z.; Jiang, X.; Wang, Y.; Li, L.; Gao, H. J.; Duan, X.; Liu, M. Possible Luttinger liquid behavior of edge transport in monolayer transition metal dichalcogenide crystals. *Nat. Commun.* **2020**, *11* (1), 659.

(22) Jaramillo, T. F.; Jorgensen, K. P.; Bonde, J.; Nielsen, J. H.; Horch, S.; Chorkendorff, I. Identification of active edge sites for electrochemical H_2 evolution from MoS_2 nanocatalysts. *Science* **2007**, *317* (5834), 100−2.

(23) Bollinger, M. V.; Lauritsen, J. V.; Jacobsen, K. W.; Norskov, J. K.; Helveg, S.; Besenbacher, F. One-dimensional metallic edge states in MoS_2. *Phys. Rev. Lett.* **2001**, *87* (19), 196803.

(24) Bollinger, M. V.; Jacobsen, K. W.; Nørskov, J. K. Atomic and electronic structure of MoS_2 nanoparticles. *Phys. Rev. B* **2003**, *67* (8), 085410.

(25) Lauritsen, J. V.; Nyberg, M.; Vang, R. T.; Bollinger, M. V.; Clausen, B. S.; Topsoe, H.; Jacobsen, K. W.; Laegsgaard, E.; Norskov, J. K.; Besenbacher, F. Chemistry of one-dimensional metallic edge states in MoS_2 nanoclusters. *Nanotechnology* **2003**, *14* (3), 385−389.

(26) Zhou, W.; Zou, X.; Najmaei, S.; Liu, Z.; Shi, Y.; Kong, J.; Lou, J.; Ajayan, P. M.; Yakobson, B. I.; Idrobo, J. C. Intrinsic structural defects in monolayer molybdenum disulfide. *Nano Lett.* **2013**, *13* (6), 2615–22.

(27) Davelou, D.; Kopidakis, G.; Kioseoglou, G.; Remediakis, I. N. MoS$_2$ nanostructures: Semiconductors with metallic edges. *Solid State Commun.* **2014**, *192*, 42–46.

(28) Gibertini, M.; Marzari, N. Emergence of One-Dimensional Wires of Free Carriers in Transition-Metal-Dichalcogenide Nanostructures. *Nano Lett.* **2015**, *15* (9), 6229–38.

(29) Wu, D.; Li, X.; Luan, L.; Wu, X.; Li, W.; Yogeesh, M. N.; Ghosh, R.; Chu, Z.; Akinwande, D.; Niu, Q.; Lai, K. Uncovering edge states and electrical inhomogeneity in MoS$_2$ field-effect transistors. *Proc. Natl. Acad. Sci. U. S. A.* **2016**, *113* (31), 8583–8.

(30) van der Zande, A. M.; Huang, P. Y.; Chenet, D. A.; Berkelbach, T. C.; You, Y.; Lee, G. H.; Heinz, T. F.; Reichman, D. R.; Muller, D. A.; Hone, J. C. Grains and grain boundaries in highly crystalline monolayer molybdenum disulphide. *Nat. Mater.* **2013**, *12* (6), 554–61.

(31) Addou, R.; Smyth, C. M.; Noh, J.-Y.; Lin, Y.-C.; Pan, Y.; Eichfeld, S. M.; Fölsch, S.; Robinson, J. A.; Cho, K.; Feenstra, R. M.; Wallace, R. M. One dimensional metallic edges in atomically thin WSe$_2$ induced by air exposure. *2D Materials* **2018**, *5* (2), 025017.

(32) Huang, T. X.; Cong, X.; Wu, S. S.; Lin, K. Q.; Yao, X.; He, Y. H.; Wu, J. B.; Bao, Y. F.; Huang, S. C.; Wang, X.; Tan, P. H.; Ren, B. Probing the edge-related properties of atomically thin MoS$_2$ at nanoscale. *Nat. Commun.* **2019**, *10* (1), 5544.

(33) Chen, Q.; Li, H.; Xu, W.; Wang, S.; Sawada, H.; Allen, C. S.; Kirkland, A. I.; Grossman, J. C.; Warner, J. H. Atomically Flat Zigzag Edges in Monolayer MoS$_2$ by Thermal Annealing. *Nano Lett.* **2017**, *17* (9), 5502–5507.

(34) Li, S.; Lin, Y. C.; Zhao, W.; Wu, J.; Wang, Z.; Hu, Z.; Shen, Y.; Tang, D. M.; Wang, J.; Zhang, Q.; Zhu, H.; Chu, L.; Zhao, W.; Liu, C.; Sun, Z.; Taniguchi, T.; Osada, M.; Chen, W.; Xu, Q. H.; Wee, A. T. S.; Suenaga, K.; Ding, F.; Eda, G. Vapour-liquid-solid growth of monolayer MoS$_2$ nanoribbons. *Nat. Mater.* **2018**, *17* (6), 535–542.

(35) Sahoo, P. K.; Memaran, S.; Xin, Y.; Balicas, L.; Gutierrez, H. R. One-pot growth of two-dimensional lateral heterostructures via sequential edge-epitaxy. *Nature* **2018**, *553* (7686), 63–67.

(36) Han, Y.; Li, M. Y.; Jung, G. S.; Marsalis, M. A.; Qin, Z.; Buehler, M. J.; Li, L. J.; Muller, D. A. Sub-nanometre channels embedded in two-dimensional materials. *Nat. Mater.* **2018**, *17* (2), 129–133.

(37) Liang, C.; Sui, X.; Wang, A.; Chang, J.; Wang, W.; Chen, Z.; Jiang, W.; Ma, Y.; Zhang, J.; Liu, X.; Zhang, Y. Controlled Production of MoS$_2$ Full-Scale Nanosheets and Their Strong Size Effects. *Advanced Materials Interfaces* **2020**, *7* (24), 2001130–2001138.

(38) Ye, S.; Xu, K.; Lei, L.; Hussain, S.; Pang, F.; Liu, X.; Zheng, Z.; Ji, W.; Shi, X.; Xu, R.; Xie, L.; Cheng, Z. Nanoscratch on single-layer MoS$_2$ crystal by atomic force microscopy: semi-circular to periodical zigzag cracks. *Materials Research Express* **2019**, *6* (2), 025048–025053.

(39) Xiao, S.-L.; Yu, W.-Z.; Gao, S.-P. Edge preference and band gap characters of MoS$_2$ and WS$_2$ nanoribbons. *Surf. Sci.* **2016**, *653*, 107–112.

(40) Tizei, L. H. G.; Lin, Y.-C.; Mukai, M.; Sawada, H.; Lu, A.-Y.; Li, L.-J.; Kimoto, K.; Suenaga, K. Exciton Mapping at Subwavelength Scales in Two-Dimensional Materials. *Phys. Rev. Lett.* **2015**, *114* (10), 107601.

(41) Susarla, S.; M. Sassi, L.; Zobelli, A.; Woo, S. Y.; Tizei, L. H. G.; Stephan, O.; Ajayan, P. M. Mapping Modified Electronic Levels in the Moire Patterns in MoS$_2$/WSe$_2$ Using Low-Loss EELS. *Nano Lett.* **2021**, *21* (9), 4071–4077.

(42) Mohn, M. J.; Hambach, R.; Wachsmuth, P.; Giorgetti, C.; Kaiser, U. Dielectric properties of graphene/MoS$_2$ heterostructures from ab initio calculations and electron energy-loss experiments. *Phys. Rev. B* **2018**, *97* (23), 235410.

(43) Kociak, M.; Kasumov, A. Y.; Guéron, S.; Reulet, B.; Khodos, I. I.; Gorbatov, Y. B.; Volkov, V. T.; Vaccarini, L.; Bouchiat, H.

Superconductivity in Ropes of Single-Walled Carbon Nanotubes. *Phys. Rev. Lett.* **2001**, *86* (11), 2416–2419.

(44) Trushin, M.; Kelleher, E. J. R.; Hasan, T. Theory of edge-state optical absorption in two-dimensional transition metal dichalcogenide flakes. *Phys. Rev. B* **2016**, *94* (15), 155301–1.

(45) D'Amico, P.; Gibertini, M.; Prezzi, D.; Varsano, D.; Ferretti, A.; Marzari, N.; Molinari, E. Intrinsic edge excitons in two-dimensional MoS$_2$. *Phys. Rev. B* **2020**, *101* (16), 161410.

(46) Qin, C.; Sandanayaka, A. S. D.; Zhao, C.; Matsushima, T.; Zhang, D.; Fujihara, T.; Adachi, C. Stable room-temperature continuous-wave lasing in quasi-2D perovskite films. *Nature* **2020**, *585* (7823), 53–57.

(47) Tsokkou, D.; Yu, X.; Sivula, K.; Banerji, N. The Role of Excitons and Free Charges in the Excited-State Dynamics of Solution-Processed Few-Layer MoS$_2$ Nanoflakes. *J. Phys. Chem. C* **2016**, *120* (40), 23286–23292.

(48) Lagarde, D.; Bouet, L.; Marie, X.; Zhu, C. R.; Liu, B. L.; Amand, T.; Tan, P. H.; Urbaszek, B. Carrier and polarization dynamics in monolayer MoS$_2$. *Phys. Rev. Lett.* **2014**, *112* (4), 047401.

(49) Wang, R.; Ruzicka, B. A.; Kumar, N.; Bellus, M. Z.; Chiu, H.-Y.; Zhao, H. Ultrafast and spatially resolved studies of charge carriers in atomically thin molybdenum disulfide. *Phys. Rev. B* **2012**, *86* (4), 045406.

(50) Glazov, M. M. Phonon wind and drag of excitons in monolayer semiconductors. *Phys. Rev. B* **2019**, *100* (4), 045426.

(51) Xu, Y.; Chen, S.; Dou, Z.; Ma, Y.; Mi, Y.; Du, W.; Liu, Y.; Zhang, J.; Chang, J.; Liang, C.; Zhou, J.; Guo, H.; Gao, P.; Liu, X.; Che, Y.; Zhang, Y. Robust production of 2D quantum sheets from bulk layered materials. *Materials Horizons* **2019**, *6* (7), 1416–1424.

(52) Vancsó, P.; Magda, G. Z.; Petö, J.; Noh, J.-Y.; Kim, Y.-S.; Hwang, C.; Biró, L. P.; Tapasztó, L. J. S. r. The intrinsic defect structure of exfoliated MoS$_2$ single layers revealed by Scanning Tunneling Microscopy. *Sci. Rep.* **2016**, *6* (1), 29726.

(53) Hong, J.; Hu, Z.; Probert, M.; Li, K.; Lv, D.; Yang, X.; Gu, L.; Mao, N.; Feng, Q.; Xie, L.; Zhang, J.; Wu, D.; Zhang, Z.; Jin, C.; Ji, W.; Zhang, X.; Yuan, J.; Zhang, Z. Exploring atomic defects in molybdenum disulphide monolayers. *Nat. Commun.* **2015**, *6* (1), 6293.

(54) Shree, S.; George, A.; Lehnert, T.; Neumann, C.; Benelajla, M.; Robert, C.; Marie, X.; Watanabe, K.; Taniguchi, T.; Kaiser, U.; Urbaszek, B.; Turchanin, A. High optical quality of MoS$_2$ monolayers grown by chemical vapor deposition. *2D Materials* **2020**, *7* (1), 015011.

(55) Kresse, G.; Furthmüller, J. Efficient iterative schemes for ab initio total-energy calculations using a plane-wave basis set. *Phys. Rev. B* **1996**, *54* (16), 11169.

(56) Perdew, J. P.; Burke, K.; Ernzerhof, M. Generalized gradient approximation made simple. *Phys. Rev. Lett.* **1996**, *77* (18), 3865.